

Coupled-cluster approach to vibronic effects in resonant inelastic x-ray scattering of quantum materials: Application to a $5d^1$ rhenium oxide

Teruki Matsuzaki,^{1,2} Liviu F. Chibotaru,^{3,*} Maristella Alessio,^{1,†} and Naoya Iwahara^{4,‡}

¹*Department of Chemistry, KU Leuven, Celestijnenlaan 200F, B-3001 Leuven, Belgium*

²*Graduate School of Science and Engineering, Chiba University,
1-33 Yayoi-cho, Inage-ku, Chiba-shi, Chiba 263-8522, Japan*

³*Theory of Nanomaterials Group, KU Leuven, Celestijnenlaan 200F, B-3001 Leuven, Belgium*

⁴*Graduate School of Engineering, Chiba University,
1-33 Yayoi-cho, Inage-ku, Chiba-shi, Chiba 263-8522, Japan*

First-principles analysis of the spectroscopic signatures of correlated quantum materials poses significant challenges due to the interplay between spin-orbit and vibronic couplings, as well as the need to describe both dynamic and static electron correlation to reach decent accuracy. In this work, we apply the equation-of-motion coupled-cluster (EOM-CC) method to derive the spin-orbit-lattice entangled vibronic states and predict the Re L_3 edge resonant inelastic x-ray scattering (RIXS) spectra of $\text{Ba}_2\text{MgReO}_6$. The EOM-CC yields interaction parameters in close agreement with those extracted from RIXS spectra, with errors of less than 5%. In particular, the EOM-CC method allowed us to determine the weak vibronic coupling to the T_{2g} vibrations, which is difficult to address experimentally. The simulated spectra indicate that vibronic coupling to the T_{2g} modes gives rise to a shoulder on the elastic peak. Going beyond the conventional treatment, which focuses solely on E_g modes, we show that vibronic couplings to both T_{2g} and E_g modes are required to account for the fine structure of the RIXS spectra. This work demonstrates that the EOM-CC method is a powerful tool for accurately predicting the complex local states at metal sites and spectroscopic signatures of correlated insulating materials.

I. INTRODUCTION

Heavy transition metal compounds host unconventional magnetism [1–9]. Over the last two decades, the iridates and ruthenates have been the playground for exploring the Kitaev spin-liquid phase and Majorana fermions. The $5d^1$ and $5d^2$ transition metal compounds have attracted recent attention as a new family of multipolar ordered materials. Unlike conventional multipolar phases observed in strongly spin-orbit coupled lanthanide and actinide compounds [10–13], in heavy transition metal compounds, the electron-phonon (vibronic) coupling affects multipolar phases.

The family of cubic $5d^1$ double perovskites exhibits various multipolar ordered phases induced by the spin-orbit and the vibronic couplings. In these compounds, the magnetic $5d^1$ metal ions in an octahedral environment form the face-centered cubic structure [Fig. 1(a)]. On each $5d^1$ center, the ligand-field and spin-orbit coupling stabilize the $j_{\text{eff}} = 3/2$ multiplet [Fig. 1(b)], causing the emergence of the multipolar nature of the ordered phases. The theories based on the spin-orbit and spin-orbital exchange interactions describe canted antiferromagnetic and antiferro-quadrupolar phase [14–16], which appears in $\text{Ba}_2\text{NaOsO}_6$ and $\text{Ba}_2\text{MgReO}_6$ at low temperature [17–21], while fail to describe the high-temperature quadrupolar phase in $\text{Ba}_2\text{MgReO}_6$ [22–24] and the ordered phase of Cs_2TaCl_6 [25, 26]. The deviation could

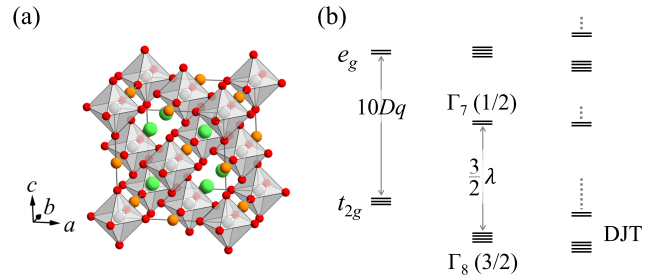


FIG. 1. The conventional unit cell of $\text{Ba}_2\text{MgReO}_6$ and the energy spectra on a $5d^1$ site. (a) The green, orange, light gray, and red spheres are Ba, Mg, Re, and O atoms, respectively. a, b, c indicate the crystal axes of the conventional cell. (b) In the descending order of energy, the ligand-field, spin-orbit coupling, and vibronic coupling (DJT effect) determine the nature of the local quantum states. $10Dq$ and λ are the ligand-field and spin-orbit coupling parameters. Γ_7 and Γ_8 are the irreducible representations of the spin-orbit multiplet $j_{\text{eff}} = 1/2$ and $j_{\text{eff}} = 3/2$ states, respectively, in the O_h group. The dots in the last column indicate the presence of a large number of vibronic levels.

arise due to vibronic effects as suggested by the structural transitions observed in $\text{Ba}_2\text{MgReO}_6$ [22–24] and Cs_2TaCl_6 [25, 26]. Density functional theory (DFT) studies also demonstrate that structural deformations are crucial for reproducing the canting angle of the magnetic moments [27, 28].

The effect of vibronic coupling on the $5d^1$ site is not limited to inducing structural deformations, but can also give rise to spin-orbit-lattice entanglement. The $j_{\text{eff}} = 3/2$ spin-orbit multiplet states couple to the Jahn-Teller

* liviu.chibotaru@kuleuven.be

† maristella.alessio@kuleuven.be

‡ naoya.iwahara@gmail.com

(JT) active vibrations (Fig. 2) of the surrounding atoms, leading to the formation of their quantum entanglement, which is the dynamic Jahn-Teller (DJT) effect [29–33]. Due to the large distance between the $5d^1$ centers in the double perovskites and the resulting weak intersite interactions, the DJT effect on the metal sites persists. In DJT systems, the energy-level distribution differs significantly from the equally spaced electronic-vibrational type [29, 33–35]. Furthermore, the DJT effect affects the nature of the multipolar moments and their orderings, which qualitatively explain the puzzling ordered phases [36].

Recent resonant inelastic x-ray scattering (RIXS) measurements unveiled the presence of the DJT effect in the $5d^1$ double perovskites. The RIXS spectroscopy is able to capture various elementary excitations [37–40], providing fundamental information on the complex energy levels of $5d$ transition metal compounds [41–46]. The RIXS spectra of the $5d^1$ double perovskites show an unexpected asymmetry of the spin-orbit $j_{\text{eff}} = 1/2$ peak and the presence of the shoulder structures near the elastic peak [47–50]. Theoretical analysis of the RIXS spectra of rhenium compounds demonstrated that these structures are the fingerprints of the JT dynamics. The asymmetric peak for the excited spin-orbit $j_{\text{eff}} = 1/2$ multiplet was detected in Re L_3 edge RIXS spectra [47], accompanied by the low-energy peaks for the transitions between the vibronic levels in oxygen K -edge RIXS spectra [50].

However, the previous theoretical analysis of the RIXS spectra could not unravel the origin of the shoulder to the elastic peak in the Re L_3 edge RIXS spectra of $\text{Ba}_2\text{MgReO}_6$ [47]. Whether the spin-orbit-lattice entangled vibronic states are sufficient to describe the $5d^1$ sites or whether other factors play a crucial role should still be clarified.

The failure in interpreting the shoulder in the Re L_3 edge RIXS spectra could stem from the insufficient knowledge of the DJT effect of the embedded $5d^1$ ion sites. The $j_{\text{eff}} = 3/2$ multiplet states couple to the two types of JT-active modes [Fig. 2], while the employed model for the analysis included only the vibronic coupling to the E_g modes [47, 50]. This approximation was motivated by the general tendency of weaker vibronic coupling of the T_{2g} modes to the d orbitals compared to the E_g modes and the difficulty in determining the weak vibronic coupling from the RIXS spectra. To unravel the true vibronic nature of the $5d^1$ sites, we must revisit the analysis of the RIXS spectra using a reliable DJT model that incorporates all relevant vibronic couplings.

To determine the DJT model, first-principles calculations are indispensable. Several groups, including us, have addressed the first-principles derivations of DJT models for embedded $5d^1$ ions using various quantum chemistry methods such as complete active space self-consistent field (CASSCF) with multireference configuration interaction (MRCI) [23, 49, 51], CASSCF with a Møller-Plesset perturbation theory [32], and DFT with Hubbard I approximation [52]. All first-principles calcu-

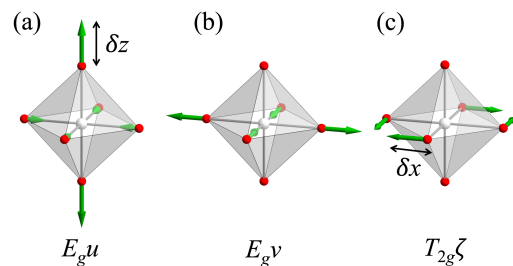


FIG. 2. The JT active modes. (a) The $E_g u$ ($= 2z^2 - x^2 - y^2$) type, (b) $E_g v$ ($= x^2 - y^2$) type, and (c) one of the T_{2g} modes ($\zeta = xy$ type), where the x, y, z directions correspond to the positive a, b, c directions in Fig. 1, respectively. Cyclic permutations of xyz obtain the other two T_{2g} modes. The green arrows indicate the displacement for the normal mode. These displacements correspond to the positive direction of the normal coordinates.

lations undertaken so far demonstrate that the vibronic coupling to the E_g modes is dominant, however, their analysis of the role of T_{2g} modes is not quantitatively conclusive.

In this work, we theoretically analyze the Re L_3 edge RIXS spectra of $\text{Ba}_2\text{MgReO}_6$. We obtain the dynamic Jahn-Teller model for $5d^1$ Re cluster with the state-of-the-art equation-of-motion coupled-cluster (EOM-CC) method. The EOM-CC method provides a robust and efficient framework for treating open-shell systems, describing the multiconfigurational character of their wavefunctions within a single-reference formalism [53–55]. The EOM-CC approach provides a balanced treatment of all relevant target states, capturing both dynamical and non-dynamical correlation within a single computational step. These methods have been extensively benchmarked for a wide range of transition-metal complexes and have demonstrated high accuracy in predicting state energies and magnetic properties [56–61]. Using the derived DJT model, we simulated the vibronic states and the Re L_3 RIXS spectra. The calculated ligand-field, spin-orbit coupling, and vibronic coupling to the E_g mode agree well with the estimated values from the Re L_3 RIXS spectra [47]. In addition, we reveal that vibronic coupling to the T_{2g} mode gives rise to a shoulder of the elastic peak of the RIXS spectra. These results illustrate the effectiveness of the EOM-CC method for exploring the nature and spectroscopic signatures of quantum materials.

II. QUANTUM STATES OF AN $5d^1$ OCTAHEDRON

A. Vibronic model Hamiltonian

We begin by reviewing the vibronic interaction in embedded $5d^1$ ions in cubic double perovskites. On the $5d^1$ sites, ligand-field, spin-orbit coupling, and vibronic coupling coexist. We describe these interactions in the

descending order of the energy scale.

Our electronic Hamiltonian for an embedded $5d^1$ metal ion consists of the ligand-field and spin-orbit coupling:

$$\hat{H}_{\text{el}} = \hat{H}_{\text{LF}} + \hat{H}_{\text{SO}}. \quad (1)$$

The ligand-field Hamiltonian splits the $5d$ orbital levels into the e_g and t_{2g} orbital levels [62]:

$$\hat{H}_{\text{LF}} = 10Dq \left(\frac{3}{5} \sum_{\gamma=u,v} |\gamma\rangle\langle\gamma| - \frac{2}{5} \sum_{\gamma=\xi,\eta,\zeta} |\gamma\rangle\langle\gamma| \right). \quad (2)$$

Here, $10Dq$ (> 0) is the ligand-field splitting parameter, and $|\gamma\rangle$ are the $5d$ orbital states. $\gamma = u, v$ indicate the basis of e_g irreducible representation, and $\gamma = \xi, \eta, \zeta$ the basis of t_{2g} representation. $\gamma = u, v, \xi, \eta, \zeta$ transform as $(2z^2 - x^2 - y^2)/\sqrt{6}$, $(x^2 - y^2)/\sqrt{2}$, $\sqrt{2}yz$, $\sqrt{2}zx$, and $\sqrt{2}xy$, respectively, under the symmetry operations of the O_h group. The octahedral ligand field makes the t_{2g} orbital levels lower than the e_g orbital levels.

\hat{H}_{SO} is the atomic spin-orbit coupling between the $5d$ orbital and spin angular momenta:

$$\hat{H}_{\text{SO}} = \lambda \sum_{\gamma\sigma} \sum_{\gamma'\sigma'} \sum_{\alpha=x,y,z} (\mathbf{l}_\alpha)_{\gamma\gamma'} \cdot (\mathbf{s}_\alpha)_{\sigma\sigma'} |\gamma\sigma\rangle\langle\gamma'\sigma'|. \quad (3)$$

Here, λ (> 0) is the spin-orbit coupling parameter, \mathbf{l}_α

($\alpha = x, y, z$) are the orbital angular momentum matrices,

$$\begin{aligned} \mathbf{l}_x &= \begin{pmatrix} 0 & 0 & \sqrt{3}i & 0 & 0 \\ 0 & 0 & i & 0 & 0 \\ -\sqrt{3}i & -i & 0 & 0 & 0 \\ 0 & 0 & 0 & 0 & i \\ 0 & 0 & 0 & -i & 0 \end{pmatrix}, \\ \mathbf{l}_y &= \begin{pmatrix} 0 & 0 & 0 & -\sqrt{3}i & 0 \\ 0 & 0 & 0 & i & 0 \\ 0 & 0 & 0 & 0 & -i \\ \sqrt{3}i & -i & 0 & 0 & 0 \\ 0 & 0 & i & 0 & 0 \end{pmatrix}, \\ \mathbf{l}_z &= \begin{pmatrix} 0 & 0 & 0 & 0 & 0 \\ 0 & 0 & 0 & 0 & -2i \\ 0 & 0 & 0 & i & 0 \\ 0 & 0 & -i & 0 & 0 \\ 0 & 2i & 0 & 0 & 0 \end{pmatrix}, \end{aligned} \quad (4)$$

with the basis orbitals $|u\rangle$, $|v\rangle$, $|\xi\rangle$, $|\eta\rangle$, $|\zeta\rangle$, \mathbf{s}_α are the $s = 1/2$ spin angular momentum matrices, and $|\gamma\sigma\rangle$ are the $5d$ spin-orbital states.

The d orbitals couple to the JT active E_g and T_{2g} modes (Fig. 2) according to the selection rule. The DJT Hamiltonian consists of the harmonic oscillator Hamiltonian for the JT active modes and the vibronic coupling:

$$\begin{aligned} \hat{H}_{\text{DJT}} &= \sum_{\Gamma=E_g, T_{2g}} \sum_{\gamma \in \Gamma} \frac{1}{2} \left(\hat{P}_\gamma^2 + \omega_\Gamma^2 \hat{Q}_\gamma^2 \right) + (|u\rangle, |v\rangle, |\xi\rangle, |\eta\rangle, |\zeta\rangle) \\ &\times \left[V_E \begin{pmatrix} -\hat{Q}_u & \hat{Q}_v & 0 & 0 & 0 \\ \hat{Q}_v & \hat{Q}_u & 0 & 0 & 0 \\ 0 & 0 & -\frac{1}{2}\hat{Q}_u + \frac{\sqrt{3}}{2}\hat{Q}_v & 0 & 0 \\ 0 & 0 & 0 & -\frac{1}{2}\hat{Q}_u - \frac{\sqrt{3}}{2}\hat{Q}_v & 0 \\ 0 & 0 & 0 & 0 & \hat{Q}_u \end{pmatrix} + V_{T_2} \begin{pmatrix} 0 & 0 & -\frac{1}{2}\hat{Q}_\xi & -\frac{1}{2}\hat{Q}_\eta & \hat{Q}_\zeta \\ 0 & 0 & \frac{\sqrt{3}}{2}\hat{Q}_\xi & -\frac{\sqrt{3}}{2}\hat{Q}_\eta & 0 \\ -\frac{1}{2}\hat{Q}_\xi & \frac{\sqrt{3}}{2}\hat{Q}_\xi & 0 & -\frac{\sqrt{3}}{2}\hat{Q}_\zeta & -\frac{\sqrt{3}}{2}\hat{Q}_\eta \\ -\frac{1}{2}\hat{Q}_\eta & -\frac{\sqrt{3}}{2}\hat{Q}_\eta & -\frac{\sqrt{3}}{2}\hat{Q}_\zeta & 0 & -\frac{\sqrt{3}}{2}\hat{Q}_\xi \\ \hat{Q}_\zeta & 0 & -\frac{\sqrt{3}}{2}\hat{Q}_\eta & -\frac{\sqrt{3}}{2}\hat{Q}_\xi & 0 \end{pmatrix} \right. \\ &+ \frac{W_E}{2} \begin{pmatrix} -\{\hat{Q}_E^2\}_u & \{\hat{Q}_E^2\}_v & 0 & 0 & 0 \\ \{\hat{Q}_E^2\}_v & \{\hat{Q}_E^2\}_u & 0 & 0 & 0 \\ 0 & 0 & -\frac{1}{2}\{\hat{Q}_E^2\}_u + \frac{\sqrt{3}}{2}\{\hat{Q}_E^2\}_v & 0 & 0 \\ 0 & 0 & 0 & -\frac{1}{2}\{\hat{Q}_E^2\}_u - \frac{\sqrt{3}}{2}\{\hat{Q}_E^2\}_v & 0 \\ 0 & 0 & 0 & 0 & \{\hat{Q}_E^2\}_u \end{pmatrix} \\ &+ \frac{W'_E}{2} \begin{pmatrix} -\{\hat{Q}_{T_2}^2\}_u & \{\hat{Q}_{T_2}^2\}_v & 0 & 0 & 0 \\ \{\hat{Q}_{T_2}^2\}_v & \{\hat{Q}_{T_2}^2\}_u & 0 & 0 & 0 \\ 0 & 0 & -\frac{1}{2}\{\hat{Q}_{T_2}^2\}_u + \frac{\sqrt{3}}{2}\{\hat{Q}_{T_2}^2\}_v & 0 & 0 \\ 0 & 0 & 0 & -\frac{1}{2}\{\hat{Q}_{T_2}^2\}_u - \frac{\sqrt{3}}{2}\{\hat{Q}_{T_2}^2\}_v & 0 \\ 0 & 0 & 0 & 0 & \{\hat{Q}_{T_2}^2\}_u \end{pmatrix} + \dots \left. \right] \begin{pmatrix} \langle u| \\ \langle v| \\ \langle \xi| \\ \langle \eta| \\ \langle \zeta| \end{pmatrix}. \quad (5) \end{aligned}$$

Here, \hat{Q}_γ and \hat{P}_γ are the mass-weighted normal coordinates and their conjugate momenta [63] for $\Gamma\gamma$ normal mode with frequency ω_Γ , and $\{\hat{Q}_\Gamma^2\}_{\gamma'}$ are the sym-

metrized products of the normal coordinates,

$$\{\hat{Q}_E^2\}_u = -\frac{1}{\sqrt{2}} \left(\hat{Q}_u^2 - \hat{Q}_v^2 \right),$$

$$\begin{aligned}
\{\hat{Q}_E^2\}_v &= \sqrt{2}\hat{Q}_u\hat{Q}_v, \\
\{\hat{Q}_{T_2}^2\}_u &= \frac{1}{\sqrt{6}}\left(-\hat{Q}_\xi^2 - \hat{Q}_\eta^2 + 2\hat{Q}_\zeta^2\right), \\
\{\hat{Q}_{T_2}^2\}_v &= \frac{1}{\sqrt{2}}\left(\hat{Q}_\xi^2 - \hat{Q}_\eta^2\right).
\end{aligned} \tag{6}$$

V_Γ are the linear vibronic coupling parameters, and W_Γ are the quadratic vibronic coupling parameters for the Γ mode.

The Re L_3 edge RIXS measurements of $\text{Ba}_2\text{MgReO}_6$ and their analysis have elucidated several interaction parameters for an embedded $5d^1$ Re ion [47], the ligand-field splitting parameter $10Dq \approx 4.5\text{-}5\text{ eV}$, the spin-orbit coupling parameter $\lambda = 0.311\text{ eV}$, and the dimensionless vibronic coupling parameter $g_E = V_E/\sqrt{\hbar\omega_E^3} = 1.325$ within the t_{2g} orbitals. See Appendix A for the dimensionless coordinates and vibronic couplings. The previous analysis of the experimental data did not provide information on the other vibronic coupling parameters, V_{T_2} , W_E , and W'_E [47].

B. Adiabatic potential energy surface and vibronic states

In this section, we discuss the nature of the vibronic eigenstates of the DJT Hamiltonian, $\hat{H}_{\text{el}} + \hat{H}_{\text{DJT}}$. To this end, we consider interactions in descending order of energy scale: the ligand field (2), spin-orbit coupling (3), and vibronic coupling (5).

The ligand-field splits the $5d$ orbital levels, and spin-orbit coupling further splits them [Fig. 1(b)]. The ligand field lowers the t_{2g} orbital level by $-4Dq$ and raises the e_g orbital level by $6Dq$. The spin-orbit coupling works within the t_{2g} orbitals and between the t_{2g} and e_g orbitals (${}^2T_{2g}$ and 2E_g term states). The spin-orbit coupling splits the six t_{2g} spin-orbital states into the $j_{\text{eff}} = 3/2$ (Γ_8) and $1/2$ (Γ_7) multiplet levels with the gap of about $3\lambda/2$, and then slightly shifts the e_g orbital levels and $j_{\text{eff}} = 3/2$ states by about $\lambda^2/10Dq$. The resulting electronic energy levels are from the lowest to the higher energy levels, $-4Dq - \frac{1}{2}\lambda$ ($j_{\text{eff}} = 3/2$), $-4Dq + \lambda$ ($j_{\text{eff}} = 1/2$), and $6Dq$ (2E_g).

The spin-orbit coupling tends to quench the vibronic coupling, while in the present case, the vibronic coupling persists in the four-fold degenerate $j_{\text{eff}} = 3/2$ quartet states [29, 30, 33]. Let us transform the electronic basis for the vibronic coupling from the t_{2g}^1 configurations into the spin-orbit multiplet states $|j_{\text{eff}}, m_j\rangle$ ($j_{\text{eff}} = 1/2, 3/2$, and $m_j = -j_{\text{eff}}, -j_{\text{eff}} + 1, \dots, j_{\text{eff}}$) [Appendix B]:

$$\begin{aligned}
\hat{V}_{\text{JT}} &= \left(\left| \frac{1}{2}, -\frac{1}{2} \right\rangle, \left| \frac{1}{2}, \frac{1}{2} \right\rangle, \left| \frac{3}{2}, -\frac{3}{2} \right\rangle, \left| \frac{3}{2}, -\frac{1}{2} \right\rangle, \left| \frac{3}{2}, \frac{1}{2} \right\rangle, \left| \frac{3}{2}, \frac{3}{2} \right\rangle \right) \\
&\times \left[V_E \begin{pmatrix} 0 & 0 & 0 & -\frac{1}{\sqrt{2}}\hat{Q}_v & 0 & \frac{1}{\sqrt{2}}\hat{Q}_u \\ 0 & 0 & -\frac{1}{\sqrt{2}}\hat{Q}_u & 0 & \frac{1}{\sqrt{2}}\hat{Q}_v & 0 \\ 0 & -\frac{1}{\sqrt{2}}\hat{Q}_u & \frac{1}{2}\hat{Q}_u & 0 & \frac{1}{2}\hat{Q}_v & 0 \\ -\frac{1}{\sqrt{2}}\hat{Q}_v & 0 & 0 & -\frac{1}{2}\hat{Q}_u & 0 & \frac{1}{2}\hat{Q}_v \\ 0 & \frac{1}{\sqrt{2}}\hat{Q}_v & \frac{1}{2}\hat{Q}_v & 0 & -\frac{1}{2}\hat{Q}_u & 0 \\ \frac{1}{\sqrt{2}}\hat{Q}_u & 0 & 0 & \frac{1}{2}\hat{Q}_v & 0 & \frac{1}{2}\hat{Q}_u \end{pmatrix} + V_{T_2} \right. \\
&\times \left. \begin{pmatrix} 0 & 0 & \frac{1}{2}\sqrt{\frac{3}{2}}(i\hat{Q}_\xi + \hat{Q}_\eta) & \frac{i}{\sqrt{2}}\hat{Q}_\zeta & \frac{1}{2\sqrt{2}}(-i\hat{Q}_\xi + \hat{Q}_\eta) & 0 \\ 0 & 0 & 0 & \frac{1}{2\sqrt{2}}(i\hat{Q}_\xi + \hat{Q}_\eta) & \frac{i}{\sqrt{2}}\hat{Q}_\zeta & \frac{1}{2}\sqrt{\frac{3}{2}}(-i\hat{Q}_\xi + \hat{Q}_\eta) \\ \frac{1}{2}\sqrt{\frac{3}{2}}(-i\hat{Q}_\xi + \hat{Q}_\eta) & 0 & 0 & -\frac{1}{2}(i\hat{Q}_\xi + \hat{Q}_\eta) & \frac{i}{2}\hat{Q}_\zeta & 0 \\ -\frac{i}{\sqrt{2}}\hat{Q}_\zeta & \frac{1}{2\sqrt{2}}(-i\hat{Q}_\xi + \hat{Q}_\eta) & -\frac{1}{2}(-i\hat{Q}_\xi + \hat{Q}_\eta) & 0 & 0 & \frac{i}{2}\hat{Q}_\zeta \\ \frac{1}{2\sqrt{2}}(i\hat{Q}_\xi + \hat{Q}_\eta) & -\frac{i}{\sqrt{2}}\hat{Q}_\zeta & -\frac{i}{2}\hat{Q}_\zeta & 0 & 0 & \frac{1}{2}(i\hat{Q}_\xi + \hat{Q}_\eta) \\ 0 & \frac{1}{2}\sqrt{\frac{3}{2}}(i\hat{Q}_\xi + \hat{Q}_\eta) & 0 & -\frac{i}{2}\hat{Q}_\zeta & \frac{1}{2}(-i\hat{Q}_\xi + \hat{Q}_\eta) & 0 \end{pmatrix} \right] \\
&\times \left(\left\langle \frac{1}{2}, -\frac{1}{2} \right|, \left\langle \frac{1}{2}, \frac{1}{2} \right|, \left\langle \frac{3}{2}, -\frac{3}{2} \right|, \left\langle \frac{3}{2}, -\frac{1}{2} \right|, \left\langle \frac{3}{2}, \frac{1}{2} \right|, \left\langle \frac{3}{2}, \frac{3}{2} \right| \right)^T.
\end{aligned} \tag{7}$$

Here, superscript T indicates transpose. We can readily

obtain the quadratic vibronic term by replacing V and

\hat{Q} in Eq. (7) with $W/2$ and $\{\hat{Q}^2\}$, respectively. The $j_{\text{eff}} = 3/2$ block of the interaction shows that the spin-orbit coupling reduces the vibronic coupling by half compared with that to the t_{2g} orbitals (5), while the vibronic coupling remains nonzero.

The nature of the ground state of the JT model depends on the adiabatic potential energy surface (APES). To grasp the fundamental information about the APES of the present system, we consider the linear vibronic coupling model within the ground $j_{\text{eff}} = 3/2$ multiplet states. For the analysis, we introduce the polar coordinates for the E_g and T_{2g} normal coordinates:

$$\begin{aligned} (Q_u, Q_v) &= \rho_E (\cos \theta_E, \sin \theta_E), \\ (Q_\xi, Q_\eta, Q_\zeta) &= \rho_{T_2} (\sin \theta_{T_2} \cos \phi_{T_2}, \sin \theta_{T_2} \sin \phi_{T_2}, \cos \theta_{T_2}). \end{aligned} \quad (8)$$

$$(\rho_E, \rho_{T_2}, U_-) = \begin{cases} (\rho_E^{\text{JT}}, 0, -E_{\text{JT},E}^{(3/2)}), & \text{for } E_{\text{JT},E}^{(3/2)} > E_{\text{JT},T_2}^{(3/2)}, \\ (\rho_E^{\text{JT}} \cos x, \rho_{T_2}^{\text{JT}} \sin x, -E_{\text{JT},E/T_2}^{(3/2)}), & \text{for } E_{\text{JT},E}^{(3/2)} = E_{\text{JT},T_2}^{(3/2)}, \\ (0, \rho_{T_2}^{\text{JT}}, -E_{\text{JT},T_2}^{(3/2)}), & \text{for } E_{\text{JT},E}^{(3/2)} < E_{\text{JT},T_2}^{(3/2)}. \end{cases} \quad (10)$$

Here, ρ_Γ^{JT} ($\Gamma = E, T_2$) are the magnitude of the JT deformation,

$$\rho_\Gamma^{\text{JT}} = \frac{V_\Gamma}{2\omega_\Gamma^2}, \quad (11)$$

$E_{\text{JT},\Gamma}^{(3/2)}$ is the depth of the APES with respect to the ground state in the absence of vibronic coupling,

$$E_{\text{JT},\Gamma}^{(3/2)} = \frac{V_\Gamma^2}{8\omega_\Gamma^2}, \quad (12)$$

and $0 \leq x \leq \pi/2$. For $E_{\text{JT},E}^{(3/2)} > E_{\text{JT},T_2}^{(3/2)}$ ($E_{\text{JT},E}^{(3/2)} < E_{\text{JT},T_2}^{(3/2)}$), the coordinates at the first and third rows in Eq. (10) correspond to the global minima and a saddle points (a saddle point and the global minima), respectively. Since the APESs of the linear vibronic model do not depend on the angle θ_E (θ_{T_2} and ϕ_{T_2}), the minimum point in Fig. 3(a) corresponds to a one-dimensional continuum of minima in the Q_θ - Q_ϵ space [Fig. 3(b)] (a two-dimensional continuum of minima in the Q_ξ - Q_η - Q_ζ space). For $E_{\text{JT},E}^{(3/2)} = E_{\text{JT},T_2}^{(3/2)}$, the APES has a continuum of minimum in the ρ_E - ρ_{T_2} space too. In this case, the minima form a four-dimensional surface in the five-dimensional coordinate space. See Refs. [29, 31, 64–67], for further information about the APES.

The previously reported linear vibronic coupling parameters [23, 49, 52] indicate that the static JT stabilization for the E_g mode is dominant in $\text{Ba}_2\text{MgReO}_6$, i.e., corresponds to the first case in Eq. (10). The APES has a one-dimensional continuum of minima (trough) which is invariant under rotation after θ_E (8) as discussed above

Diagonalizing the potential term, we obtain the analytical expressions for the APES.

$$U_\pm = \frac{\omega_E^2}{2} \rho_E^2 + \frac{\omega_{T_2}^2}{2} \rho_{T_2}^2 \pm \frac{1}{2} \sqrt{V_E^2 \rho_E^2 + V_{T_2}^2 \rho_{T_2}^2}. \quad (9)$$

Each APES represents a set of Kramers doublet levels. As Eq. (9) shows, the APES is independent of the angles in the polar coordinates (8) within the linear vibronic approximation.

Let us analyze the structure of the APES. Figure 3(a) is a plot of U_\pm . In ρ_E - ρ_{T_2} coordinate space, the positions and the values of the extrema of U_\pm are

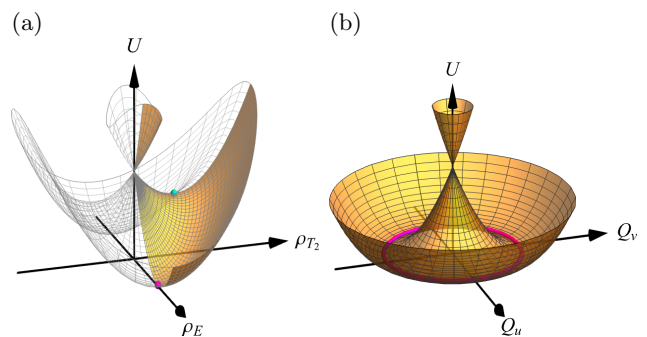


FIG. 3. The adiabatic potential energy surface (APES) for the linear JT model within the $j_{\text{eff}} = 3/2$ multiplet states. (a) U_\pm with respect to ρ_E and ρ_{T_2} (9). The magenta and cyan points indicate the minimum and the saddle points, respectively. The plot shows the case for $E_{\text{JT},E}^{(3/2)} > E_{\text{JT},T_2}^{(3/2)}$. (b) The angular dependence of the continuum of minima of E_g type. This forms a circle (red) around the high-symmetric point. In both plots, the origin of the coordinates corresponds to the degeneracy point of the ground electronic state.

[Fig. 3(b)]. The higher-order vibronic and the pseudo JT-type vibronic couplings warp this trough, generating three equivalent minima at the tetragonally compressed structures along one of the three crystallographic axes [Fig. 1(a)]. We will examine the impact of these interactions on the APES in Sec. IV B using the first-principles interaction parameters for a Re ion site in $\text{Ba}_2\text{MgReO}_6$.

The low-energy vibronic eigenstates of $\hat{H}_{\text{el}} + \hat{H}_{\text{DJT}}$ delocalize over the three minima of the APES. The vibronic wavefunctions basically spread over the warped trough,

which leads to the additional stabilization with respect to the one arising from the static JT deformation ($\rho_E > 0$) [29, 34]. The vibronic coupling to the T_{2g} modes perturbs the low-energy vibronic states by allowing a slight delocalization of the wave functions over the saddle points of the APES [Fig. 3(a)]. We will analyze the nature of the vibronic states on Re sites of $\text{Ba}_2\text{MgReO}_6$ in Sec. IV B.

The vibronic states are characterized by the quantum entanglement of the spin-orbit and lattice vibrational degrees of freedom and take the following form [29, 30, 34]:

$$|\Psi_\nu\rangle = \sum_i |\psi_i\rangle \otimes |\chi_{i\nu}\rangle, \quad (13)$$

where $|\psi_i\rangle$ are the electronic eigenstates, and $|\chi\rangle$ correspond to the lattice part. We further determine $|\Psi_\nu\rangle$ in Eq. (13) by solving the corresponding vibronic eigenvalue problem using the first-principles calculated vibronic parameters.

III. COMPUTATIONAL DETAILS

A. Electronic states

We calculated the electronic states of a cluster of $\text{Ba}_2\text{MgReO}_6$ using the equation-of-motion coupled-cluster singles and doubles (EOM-CCSD) method. We performed all electronic state calculations using the Q-Chem package (version 6.1) [68].

The cluster (Fig. 4) is extracted from the experimental crystal structure [69]. The cluster consists of a central ReO_6 octahedron, its nearest neighboring diamagnetic ions (eight Ba and six Mg atoms), and point charges representing the surrounding ions. We treated the $\text{Ba}_8\text{Mg}_6\text{ReO}_6$ cluster quantum chemically. For these atoms, we employed contracted basis sets as follows: For the Re ion, an all-electron type of the exact two-component triple zeta valence and polarization (X2C-TZVP) [70], for the nearest neighbor six oxygen ligand atoms, the correlation-consistent polarized valence triple zeta (cc-pVTZ) basis set [71], and, for the next nearest neighbor Ba and Mg ions, Stevens, Basch, Krauss, Jasien, and Cundari's valence double zeta (SBKJC-VDZ) type with the corresponding effective core potentials [72, 73]. These basis sets were obtained from the Basis Set Exchange [74]. For the Re cluster, scalar relativistic effects are further included via spin-free exact two-component theory in its one-electron variant (SFX2C-1e) [75–77]. To account for the contribution from the crystal environment, we replaced all remaining 1420 ions in a supercell composed of $3 \times 3 \times 3$ conventional cells with point charges. As charges, we adopted Mulliken charges of Re: +1.24, O: -1.10, Ba: +1.84, and Mg: +2.11.

To describe the $5d^1$ electronic states of the Re cluster, we employed the electron-attachment (EA) approach [78], in which an extra electron is attached to a $5d^0$ reference state. Core electrons were frozen in all calculations.

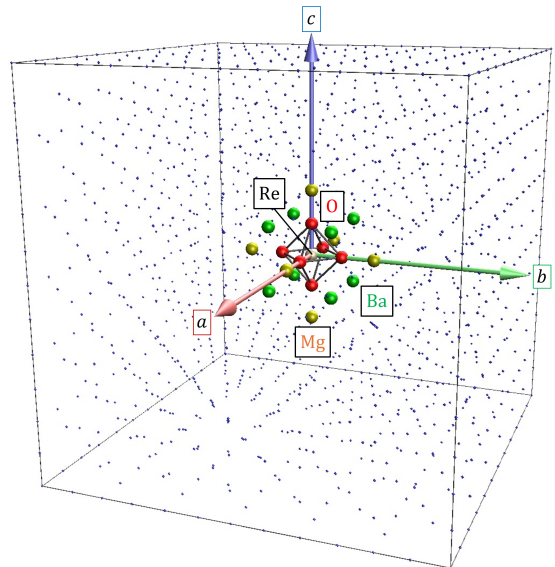


FIG. 4. The rhenium cluster embedded in 1420 point charges. The cluster consists of ReO_6 and the six nearest Mg and eight nearest Ba ions. The quantum-mechanical cluster is cut out from the crystallographic structure. The blue dots represent the point charges.

We computed two sets of degenerate term states: ${}^2T_{2g}$ and 2E_g . The energy gap between them corresponds to $10Dq$.

Using the EOM-CCSD wave functions, we computed the spin-orbit couplings as matrix elements of the Breit-Pauli spin-orbit Hamiltonian, as implemented in the Q-Chem package [57, 79, 80]. This implementation relies on a mean-field treatment of the two-electron terms and uses the Wigner-Eckart theorem, applied to reduced one-particle density matrices, to derive spin-orbit couplings between all multiplet components [57]. We fitted Eq. (3) to these matrix elements between the ${}^2T_{2g}$ term states and obtained the spin-orbit coupling parameter λ .

B. Vibronic coupling parameters

We derived the vibronic coupling parameters and frequencies from the EOM-CC APES with respect to the JT-active modes. The Cartesian coordinates for the JT deformed structures of the $5d$ metal clusters were calculated by [63]

$$\mathbf{R}_A = \mathbf{R}_A^0 + Q_\alpha \frac{\mathbf{u}_A^\alpha}{\sqrt{M_A}}, \quad (14)$$

where \mathbf{R}_A are the Cartesian coordinates of atom A in the cluster, \mathbf{R}_A^0 the coordinates without the JT deformations corresponding to the experimental structure, \mathbf{u}_A^α the normalized eigenvectors of the dynamical matrix, and M_A the mass of atom A . To derive the frequencies and the vibronic couplings to the E_g (T_{2g}) modes, we set $Q_u \neq 0$ ($Q_\zeta \neq 0$) and the others to zero. These parameters were

obtained by fitting the EOM-CCSD ${}^2T_{2g}$ term levels to the potential energy in Eq. (5).

The dimensions of the physical quantities are as follows. The dimensions of \mathbf{R} , M_A , and Q_α are Bohr radius (a_0), the mass of electron (m_e), and $a_0\sqrt{m_e}$. The dimension of the linear vibronic coupling parameters is $E_h/a_0\sqrt{m_e}$, and of the quadratic vibronic coupling parameters and frequency are $E_h/a_0^2m_e$ and $\sqrt{E_h/a_0^2m_e}$, respectively, where E_h is the Hartree energy. For the vibronic coupling parameters, we also use the dimensionless parameters (see Appendix A).

C. Vibronic states

We calculated the vibronic states by numerically diagonalizing the model vibronic Hamiltonian, $\hat{H}_{\text{el}} + \hat{H}_{\text{DJT}}$. To this end we expanded $|\chi\rangle$ in Eq. (13) into eigenstates of the harmonic oscillator [30, 34, 35]:

$$|\chi_{i\nu}\rangle = \sum_{n_u, n_v, n_\xi, n_\eta, n_\zeta=0}^{\infty} |n_u, n_v, n_\xi, n_\eta, n_\zeta\rangle \chi_{in;\nu}, \quad (15)$$

where $|n_u, n_v, n_\xi, n_\eta, n_\zeta\rangle$ are the eigenstates of the harmonic oscillator part in \hat{H}_{DJT} , n_γ ($= 0, 1, 2, \dots$) are the vibrational quantum numbers for the mode γ , $\mathbf{n} = (n_u, n_v, n_\xi, n_\eta, n_\zeta)$, and $\chi_{in;\nu} = \langle \mathbf{n} | \chi_{i\nu} \rangle$. With the vibronic basis of $|\psi_i\rangle \otimes |n_u, n_v, n_\xi, n_\eta, n_\zeta\rangle$, we constructed the vibronic Hamiltonian matrix.

We employed a sufficiently large vibronic basis that can accurately describe the vibronic states and thereby explain the experimental data. In our vibronic basis, the vibrational quanta fulfill

$$\begin{aligned} n_u + n_v + n_\xi + n_\eta + n_\zeta &\leq 7, \\ n_u + n_v &\leq 5, \quad n_\xi + n_\eta + n_\zeta \leq 4. \end{aligned} \quad (16)$$

We checked the convergence of the energy with respect to the size of the vibrational basis. With the DJT model including only the E_g (T_{2g}) modes, the ground vibronic level changes by less than 10^{-5} eV by increasing the maximum vibrational number to 5 (4).

For the calculations of the vibronic states, we used in-house program code.

D. RIXS spectra

The obtained vibronic eigenstates were used to simulate the Re L_3 edge RIXS spectra. In the RIXS process, the embedded Re ion absorbs one photon accompanied by an electronic excitation from $2p_{3/2}$ to $5d$ orbitals, and then emits one photon with the electron transition from a $5d$ orbital to the empty $2p$ orbital. The initial and final states of the $5d^1$ Re ion are of vibronic type.

We calculate the scattering intensity using the Kramers-Heisenberg formula [37, 81]. Under the resonant

condition, the intensity is, in a good approximation,

$$I_{fi}(\omega_f) \propto \left| \sum_n \frac{(\boldsymbol{\varepsilon}^{(f)} \cdot \langle \Psi_f | \hat{\mathbf{p}} | n \rangle)(\boldsymbol{\varepsilon}^{(i)} \cdot \langle n | \hat{\mathbf{p}} | \Psi_i \rangle)}{\hbar\omega_i + E_i - E_n + i\frac{\Gamma}{2}} \right|^2 \times \delta(\hbar\omega_i + E_i - \hbar\omega_f - E_f). \quad (17)$$

Here, $\boldsymbol{\varepsilon}^{(i)}$ and $\boldsymbol{\varepsilon}^{(f)}$ are the polarization vectors of the incident and scattered photons, and the corresponding photon energies are $\hbar\omega_i$ and $\hbar\omega_f$; the initial ($|\Psi_i\rangle$) and final ($|\Psi_f\rangle$) states are vibronic states of the $5d^1$ octahedron, and $|n\rangle$ are the intermediate states with one core-hole in $2p_{3/2}$, Γ being the core-hole lifetime. To illustrate the vibronic effect, we compare the spectra arising from the transition between vibronic and pure electronic eigenstates in both the initial and final states.

We approximate the structure of the intermediate states in Eq. (17) as follows. The imaginary part ($\Gamma/2$) of Eq. (17) for the $2p_{3/2}$ core-hole states of $5d$ metal ions in insulators amounts to as much as 2.75 eV [82]. The real part depends on the type of the $5d^2$ electron configurations. The t_{2g}^2 configurations are close to the resonant condition, leaving only the imaginary part as the denominator of Eq. (17). The energies of the $t_{2g}^1e_g^1$ configurations are about $10Dq$ higher than those of the t_{2g}^2 configurations, and the real part is comparable to the imaginary part. Within this approximation the cross-section reduces to

$$I_{fi} \propto |G_f|^2 \left| \sum_n (\boldsymbol{\varepsilon}^{(f)} \cdot \langle f | \hat{\mathbf{p}} | n \rangle)(\boldsymbol{\varepsilon}^{(i)} \cdot \langle n | \hat{\mathbf{p}} | i \rangle) \right|^2 \times \delta(\hbar\omega_i + E_i - \hbar\omega_f - E_f), \quad (18)$$

where G_f is the approximate core-hole propagator:

$$|G_f| = \begin{cases} |\Gamma/2|^{-1}, & \text{for the } t_{2g} \text{ peaks} \\ |10Dq + i\Gamma/2|^{-1}. & \text{for the } e_g \text{ peaks} \end{cases} \quad (19)$$

We use Eq. (18) for the calculations of the L_3 edge RIXS spectra.

Further ingredients for simulating RIXS spectra comply with the experimental conditions [47]. Thus, we used the experimental scattering geometry; the wave vectors of the incident (\mathbf{k}_i) and scattered (\mathbf{k}_f) photons are perpendicular to each other, and $\mathbf{k}_f - \mathbf{k}_i \parallel [111]$. The incident and scattered photons are π -polarized. Given that the temperature dependence of the L_3 RIXS spectra is minor below 40 K, the RIXS spectra were simulated at $T = 0$ K. We assumed the Re sites to be completely octahedral because tiny deformations under the quadrupolar ordering do not give significant influence on the shape of the RIXS spectra when averaged over the three domains [50] (for domains in $\text{Ba}_2\text{MgReO}_6$, see Ref. [24]). Finally, we broaden the spectra by convoluting the intensities with Gaussian functions.

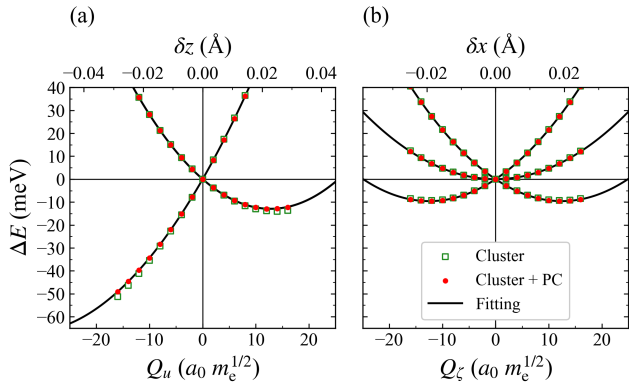


FIG. 5. The ${}^2T_{2g}$ adiabatic potential energy surfaces with respect to (a) the E_{gu} and (b) the $T_{2g}\zeta$ deformations. The green squares, the red points, and the black solid lines are, respectively, the ${}^2T_{2g}$ levels of the Re cluster without surrounding point charges, those of the Re cluster with surrounding point charges (PC), and the adiabatic potential energy surfaces of the model Hamiltonian. We show the displacements of the oxygen atoms by the JT active modes. For δz and δx , see Fig. 2.

TABLE I. Coupling parameters for the $5d^1$ Re cluster. The ligand-field and spin-orbit coupling parameters are in eV, and the frequencies and the static and DJT stabilization energies are in meV. The vibronic coupling parameters are dimensionless (See Appendix A). $E_{JT}^{(3/2)}$ corresponds to Eq. (12), E_{JT} is the static JT stabilization energy extracted from the APES, which includes the pseudo JT type vibronic coupling effects, and E_{DJT} is the stabilization energy by the DJT effect. Figure 6 shows $E_{JT}^{(3/2)}$ and E_{JT} , and Fig. 7 shows E_{DJT} .

Method	EOM-CCSD This work	DFT+HI [52]	MRCI [23]	RIXS [47]			
Electronic parameters							
$10Dq$	4.88	4.5					
λ	0.321	0.29		0.311			
Vibronic coupling parameters							
Γ	E_g	T_{2g}	E_g	T_{2g}	E_g	T_{2g}	E_g
ω_Γ	63.1	55.6	75.3	49.8			67.3
g_Γ	1.332	0.71	1.20	0.84			1.325
w_Γ	0.23	-0.21					
$E_{JT,\Gamma}^{(3/2)}$	14.2	4.4	13.6	4.4	11 ^a	3 ^a	14.7
$E_{JT,\Gamma}$	20.4	4.5					19.1 ^b
E_{DJT}	38.5						31.5 ^c

^a 1/4 of the reported JT energies for the ${}^2T_{2g}$ term.

^b Calculated data with $w_E = 0$.

^c Calculated data with $g_{T_2} = 0$ and $w_E = 0$.

IV. RESULTS AND DISCUSSION

A. Electronic and vibronic interaction parameters

We derived the ligand-field parameter from the EOM-CCSD levels and the spin-orbit coupling parameters by mapping the spin-orbit coupling matrix to Eq. (3). Table I shows the electronic interaction parameters. The

energy gap between the ground $j_{\text{eff}} = 3/2$ multiplet level and the e_g level is about $10Dq + \lambda/2 \approx 5.04$ eV, which is in line with the e_g peak position (4.5-5 eV) in the Re L_3 edge RIXS spectra [47, 49]. The spin-orbit coupling parameter of 0.321 eV is close to 0.311 eV extracted from the RIXS spectra [47].

The frequencies and vibronic coupling parameters were derived from the EOM-CCSD adiabatic potential energy surface. As described in Sec. III A, we deformed the Re cluster using the JT active modes and calculated the EOM-CC energy levels at each deformed structure. Figure 5 shows the APESs with respect to the E_g and the T_{2g} JT deformations. We verified that the present approach gives the frequencies with an accuracy of 5% by using a diamagnetic analog where Raman scattering data are available [83] (Appendix C).

Table I lists the calculated frequencies and the vibronic coupling parameters for the embedded Re clusters. Moreover, the vibronic coupling parameter for the E_g mode ($g_E = 1.332$) agrees well with the value extracted from the RIXS spectra ($g_E = 1.325$) [47]. The calculated vibronic coupling parameter for the T_{2g} mode ($g_{T_2} = 0.71$) shows that the coupling is weaker than that for the E_g mode but is nonnegligible: In terms of the static JT energy [$E_{JT}^{(3/2)}$, Eq. (12)], the vibronic coupling to the T_{2g} mode amounts to about 30% of that to the E_g mode. The strengths of the vibronic couplings and $E_{JT}^{(3/2)}$'s align with previous calculations using DFT + Hubbard I (DFT+HI) [52], and MRCI [23, 49] approaches. To evaluate the reliability of the calculated vibronic couplings to the T_{2g} mode, a comparison with experimental data is necessary.

Note that the point charges do not give a large influence on the interaction parameters. Without the point charges, we obtained $10Dq = 4.80$ eV, $\lambda = 0.322$ eV, $\omega_E = 61.5$ meV, $g_E = 1.408$, $w_E = 0.25$, $\omega_{T_2} = 56.1$ meV, $g_{T_2} = 0.69$, and $w_{T_2} = -0.21$ (see Fig. 5 for the vibronic couplings and frequencies). g_E shows the largest deviation of 6% from the data with the point charges.

Using the EOM-CC method, we obtained the interaction parameters for $5d^1$ sites in $\text{Ba}_2\text{MgReO}_6$. The calculated parameters are in agreement with those from the Re L_3 edge RIXS spectra [47], which illustrates the reliability of our approach. Furthermore, the present approach allows us to extend the model for the embedded Re cluster by including the vibronic coupling to the T_{2g} modes, which have not been extracted from experimental data. We examine the validity of the derived vibronic model by simulating the Re L_3 edge RIXS spectra in Sec. IV C.

B. Static and DJT effects

Now we are in a position to quantitatively analyze the static and the DJT effect on Re sites. We begin by analyzing the APES of the derived model.

Figure 6 shows the $j_{\text{eff}} = 3/2$ APESs for the E_g and the T_{2g} deformations. To clarify the impact of the quadratic vibronic coupling and pseudo JT coupling between the

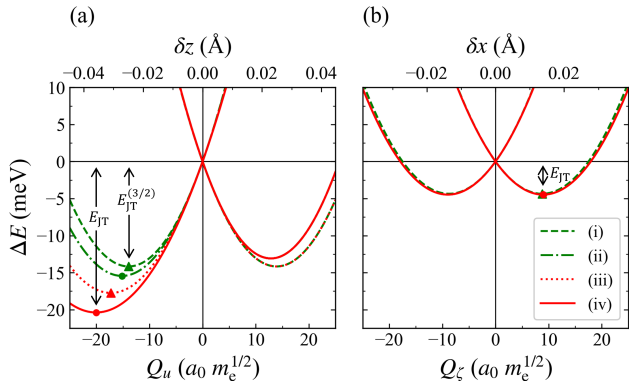


FIG. 6. The $j_{\text{eff}} = 3/2$ adiabatic potential energy surfaces with respect to (a) the E_g deformations and (b) the T_{2g} deformations. (i) without quadratic vibronic and pseudo JT (the green dashed line), (ii) with quadratic vibronic but without pseudo JT (the green dash-dotted line), (iii) without quadratic vibronic but with pseudo JT (the red dotted line), (iv) with both the quadratic and pseudo JT couplings (the red solid line). For the vibronic models, we used the parameters from the present EOM-CCSD calculations. $E_{\text{JT}}^{(3/2)}$ is the static JT energy of model (i) [Eq. (12)], and E_{JT} is the stabilization energy of model (iv).

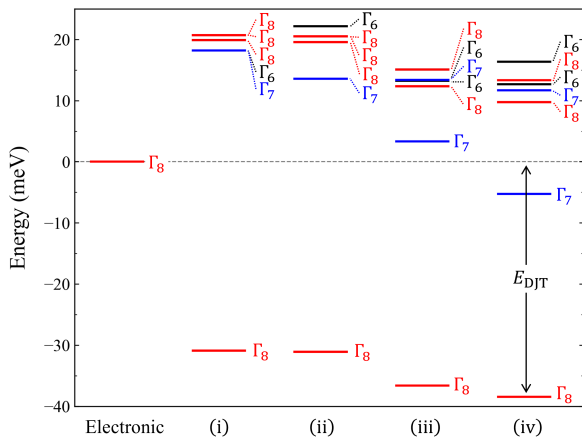


FIG. 7. The vibronic levels (meV) for DJT models (i)-(iv). Γ_6 , Γ_7 , and Γ_8 are the irreducible representations of the vibronic states within the O_h group. We set the ground-state energy, in the absence of vibronic coupling, to zero. E_{DJT} is the stabilization energy by the DJT effect.

$j_{\text{eff}} = 3/2$ and $1/2$ on the JT effect, we analyzed four models: (i) without pseudo JT and quadratic (the green dashed line), (ii) without pseudo JT but with quadratic (the green dash-dotted line), (iii) with pseudo JT and without quadratic (the red dotted line), and (iv) with both pseudo JT and quadratic (the red solid line) couplings. The APES of the linear vibronic model (i) has a continuum of minima in the Q_u - Q_v space with depth of $E_{\text{JT},E}^{(3/2)}$ (12). The quadratic vibronic and the pseudo JT couplings further stabilize the tetragonally compressed states [Fig. 2(a)] by 1.3 meV and 3.6 meV, respectively.

Both couplings to the E_g modes enhance the JT deformation in model (iv), for which the total JT stabilization energy ($E_{\text{JT},E}$) is by 6.2 meV larger than $E_{\text{JT},E}^{(3/2)}$. At the minima of the APES within model (iv), the Re-O bond length along one of the crystallographic axes is compressed by 0.036 Å.

The APES with respect to the T_{2g} deformations shows that the quadratic and the pseudo JT couplings involving the T_{2g} modes are negligible [Fig. 2(c)]: $E_{\text{JT},T_2} \approx E_{\text{JT},T_2}^{(3/2)}$. Nonlinear vibronic effects become sizable when the linear vibronic coupling is large, which is not the case here. Hereafter, we omit the nonlinear vibronic couplings related to the T_{2g} modes.

Quantization of the lattice degrees of freedom in the JT model leads to the stabilization of the spin-orbit-lattice entangled states. We numerically diagonalized the DJT model ($\hat{H}_{\text{el}} + \hat{H}_{\text{DJT}}$) as described in Sec. III C and obtained the energies of these states. The ground-state energies of models (i)-(iv) and model (iv) with $V_{T_2} = 0$ are stabilized by, respectively, 30.9, 31.1, 36.6, 38.5, and 29.3 meV compared with the ground-state energy of the model without vibronic coupling (Fig. 7). The most significant contribution to the DJT stabilization energy comes from the linear vibronic coupling to the E_g modes. The second largest contribution of ≈ 9.2 meV comes from the linear vibronic coupling to the T_{2g} modes. Then the pseudo JT and the quadratic couplings stabilize the system by about 5.7 meV and 0.2 meV, respectively.

As suggested from the contributions to the DJT stabilization, the vibronic coupling to the T_{2g} modulates the nature of the ground vibronic state. In the ground vibronic states [Eq. (D1)], the vibronic basis states involving $j_{\text{eff}} = 3/2$ and one T_{2g} vibrational excitation amount to as much as 7%, which is not negligible compared with the contribution of 20 % from the one E_g vibrational excitation.

Figure 7 shows how the low-energy vibronic levels evolve with respect to the quadratic vibronic coupling and pseudo JT coupling. Some of the low-energy vibronic states are $\Gamma_8 \otimes E$ type, and the others are the hybrid $\Gamma_8 \otimes (E \oplus T_2)$ type. The first and second excited (Γ_7 and Γ_6) levels of model (i) are of the first type [Eq. (D5)]. Introducing the warping of the APES with the quadratic vibronic and the pseudo JT couplings, the Γ_7 vibronic level lowers [84], approaching the tunneling splitting type excitation in strongly warped APES [29, 33]. The higher excited vibronic states typically exhibit a hybrid character arising from a mixing of the E_g - and T_{2g} -type vibrational excitations (the second type). The first excited Γ_8 vibronic states above the Γ_7 level (Fig. 7) are mainly of one T_{2g} vibration type, $|j_{\text{eff}} = 3/2 m_j\rangle \otimes |0, 0, n_\xi, n_\eta, n_\zeta\rangle$ with $n_\xi + n_\eta + n_\zeta = 1$, while these states also have non-negligible contributions from the E_g vibrationally excited vibronic basis [Eq. (D6)].

From the analysis of the JT effect considering both E_g and T_{2g} modes, we showed that the vibronic coupling to the T_{2g} modes gives a nonnegligible contribution to the JT energy (about 20%) and modulates the nature of the

vibronic wave functions.

C. RIXS spectra

With the obtained vibronic states, we simulated the Re L_3 edge RIXS spectra (Figure 8). The electronic RIXS spectra (represented by the green solid lines) have a symmetric peak for each of the electronic levels: the elastic peak at 0 eV, the inelastic peak for $j_{\text{eff}} = 1/2$ at 0.5 eV, and the inelastic peak for e_g (2E_g) at 5.1 eV. Turning on the vibronic coupling to the E_g modes, the $j_{\text{eff}} = 1/2$ peak and the e_g peak shift, and their shapes become asymmetric as reported before (the blue solid lines) [47, 50]. Then, including vibronic coupling to the T_{2g} modes [model (iv)], the elastic peak shows a clear shoulder below 0.3 eV (the red solid lines). The low-energy shoulder is in good agreement with the experimentally detected feature in Ref. [47].

The vibronic coupling shifts the peak positions of the $j_{\text{eff}} = 1/2$ and the e_g peaks. The DJT effect stabilizes the ground $j_{\text{eff}} = 3/2$ and the 2E_g states. The vibronic coupling of the pseudo JT type widens the spin-orbit multiplet levels. Thus, the $j_{\text{eff}} = 1/2$ peak exhibits a shift towards the higher energy by about 50 meV, while the 2E_g peak does towards the lower energy. The errors of the calculated peak positions with respect to the experimental ones [47] are within 10%: The peaks for the $j_{\text{eff}} = 1/2$ and 2E_g are about 50 meV and 0.5 eV higher than the experimental peaks at 0.50 eV and 4.56 eV, respectively [47].

Figure 9 highlights in color the vibronic levels that contribute strongly to the transitions. The asymmetric peaks of the vibronic RIXS spectra come from the multitude of transitions from the ground to the excited vibronic states. The mechanism is similar to Franck-Condon's for shifted oscillators: a multitude of excitations from the ground to the excited vibronic levels give rise to the asymmetric peaks. One can find a detailed description of the asymmetric $j_{\text{eff}} = 1/2$ peak in Refs. [47, 50]. The broad shoulder of the elastic peak appears due to the transitions from the ground vibronic levels to the excited vibronic levels that mainly arise from the T_{2g} vibrational excitations, Eq. (D6).

With the present model, we have reproduced all the essential features of the Re L_3 edge RIXS spectra. In particular, the shoulder peak arises from the vibronic coupling to the T_{2g} modes, which was missing in earlier models.

V. CONCLUSION

In this work, we investigated the DJT effect for $5d^1$ Re sites in $\text{Ba}_2\text{MgReO}_6$ by using the EOM-CC method, and simulated the Re L_3 edge RIXS spectra. The calculated ligand-field splitting, spin-orbit coupling, and vibronic

couplings are in close agreement with the reported experimental data [47]: The discrepancies are within 5%, which illustrates the reliability of the adopted CC approach. From the simulated RIXS spectra, the shoulder on the elastic peak is induced by the vibronic coupling to the T_{2g} vibrations, which was not assigned in the previous analysis due to the neglect of T_{2g} vibrational degrees of freedom. The present results illustrate that, for a unified quantitative description of the multipolar features of the family of $5d^1$ double perovskites, the DJT effect is crucial.

The present work also demonstrates the usefulness of the EOM-CC method in elucidating the local vibronic model and analyzing the RIXS spectra of the $5d$ compound. The present protocol using the EOM-CC method opens an avenue to accurate theoretical predictions of the complex electronic states of various correlated quantum materials and their spectroscopic signatures.

ACKNOWLEDGMENTS

T.M. and N.I. are grateful to the Division of Quantum and Physical Chemistry at KU Leuven for hospitality. The work at Chiba was partly supported by Grant-in-Aid for Scientific Research (Grant No. 22K03507) from the Japan Society for the Promotion of Science, the Nippon Sheet Glass Foundation for Materials Science and Engineering, and the JST CREST project led by T. Omatsu (No. JPMJCR1903).

DATA AVAILABILITY

The data that support the findings of this article are openly available [85].

Appendix A: Dimensionless vibronic quantities

Dimensionless vibronic coupling parameters are convenient for theoretical descriptions of the DJT effect. We transform the mass-weighted normal coordinates and the conjugate momenta [63] into the dimensionless coordinates and momenta, respectively, by the following relations:

$$\hat{Q}_\gamma = \sqrt{\frac{\hbar}{\omega_\Gamma}} \hat{q}_\gamma, \quad \hat{P}_\gamma = \sqrt{\hbar\omega_\Gamma} \hat{p}_\gamma. \quad (\text{A1})$$

The dimensionless coordinates and momenta are, in terms of the vibrational creation and annihilation operators (\hat{b}_γ^\dagger and \hat{b}_γ),

$$\hat{q}_\gamma = \frac{1}{\sqrt{2}} (\hat{b}_\gamma^\dagger + \hat{b}_\gamma), \quad \hat{p}_\gamma = \frac{i}{\sqrt{2}} (\hat{b}_\gamma^\dagger - \hat{b}_\gamma). \quad (\text{A2})$$

Substituting them into the vibronic Hamiltonian, the Hamiltonian reduces to the form of the products of the

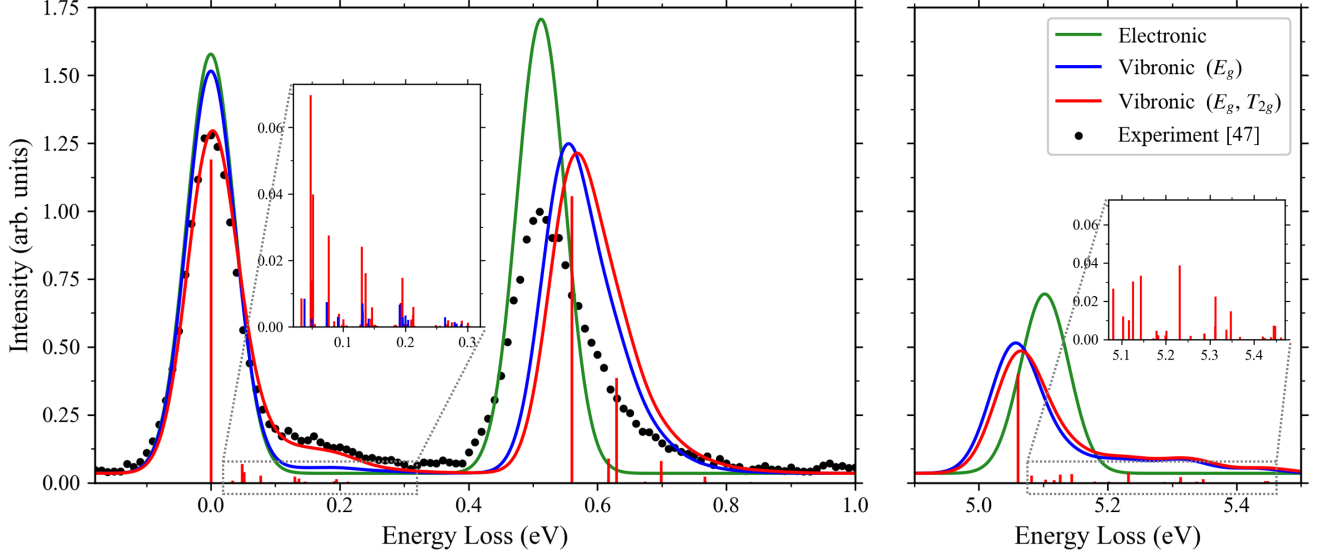


FIG. 8. Simulated Re L_3 edge RIXS spectra. The green solid lines are the electronic RIXS spectra. The blue and red solid lines represent the vibronic RIXS spectra based on models that include only the E_g mode and both the E_g and T_{2g} modes, respectively. The black points are the experimental data and taken from Ref. [47]. The insets show the intensities that contribute to the shoulders of the elastic scattering and the t_{2g} - e_g transition.

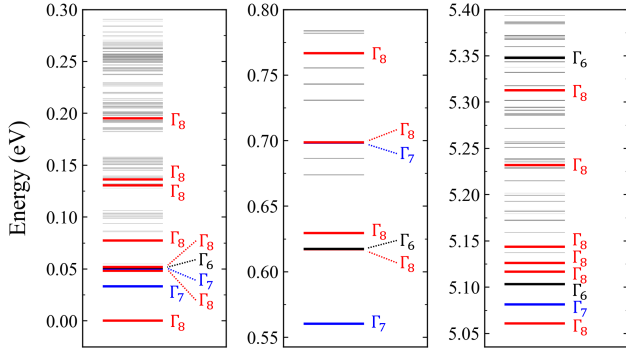


FIG. 9. The assignment of the RIXS vibronic transitions. The thick lines indicate the vibronic levels relevant to the strong RIXS intensities. The thick black, blue, and red lines are the Γ_6 , Γ_7 , and Γ_8 irreducible representations. We set the ground level to zero in this figure.

frequency ($\hbar\omega$) and dimensionless operator. The latter contains dimensionless vibronic coupling parameters defined by

$$g_\Gamma = \frac{V_\Gamma}{\sqrt{\hbar\omega_\Gamma^3}}, \quad w_E = \frac{W_E}{\omega_E^2}, \quad w'_E = \frac{W'_E}{\omega_{T_2}^2}. \quad (\text{A3})$$

We obtain a dimensionless form of the vibronic Hamiltonian by replacing V (W) and \hat{Q} with $\hbar\omega g$ ($\hbar\omega w$) and \hat{q} , respectively.

Appendix B: t_{2g}^1 configurations and spin-orbit multiplet states

The relation between the t_{2g}^1 electronic configurations and the spin-orbit multiplet states is

$$|j_{\text{eff}}, m_j\rangle = \sum_{\gamma\sigma} |\gamma\sigma\rangle (\Gamma_5\gamma, \Gamma_6\sigma | j_{\text{eff}}, m_j), \quad (\text{B1})$$

where Clebsch-Gordan coefficients for the O_h group, $(\Gamma_5\gamma, \Gamma_6\sigma | j_{\text{eff}}, m_j)$ [86], were used; $j_{\text{eff}} = 1/2$ and $3/2$ are, respectively, Γ_7 and Γ_8 representations. The explicit forms of the relation are as follows:

$$\left(\left| \frac{1}{2}, -\frac{1}{2} \right\rangle, \left| \frac{1}{2}, \frac{1}{2} \right\rangle, \left| \frac{3}{2}, -\frac{3}{2} \right\rangle, \left| \frac{3}{2}, -\frac{1}{2} \right\rangle, \left| \frac{3}{2}, \frac{1}{2} \right\rangle, \left| \frac{3}{2}, \frac{3}{2} \right\rangle \right) = (|\xi, \downarrow\rangle, |\xi, \uparrow\rangle, |\eta, \downarrow\rangle, |\eta, \uparrow\rangle, |\zeta, \downarrow\rangle, |\zeta, \uparrow\rangle) \mathbf{U}, \quad (\text{B2})$$

$$\mathbf{U} = \begin{pmatrix} 0 & -\frac{i}{\sqrt{3}} & 0 & -\frac{1}{\sqrt{3}} & \frac{i}{\sqrt{3}} & 0 \\ -\frac{i}{\sqrt{3}} & 0 & \frac{1}{\sqrt{3}} & 0 & 0 & -\frac{i}{\sqrt{3}} \\ -\frac{i}{\sqrt{6}} & 0 & \frac{1}{\sqrt{6}} & 0 & 0 & i\sqrt{\frac{2}{3}} \\ 0 & \frac{i}{\sqrt{2}} & 0 & -\frac{1}{\sqrt{2}} & 0 & 0 \\ -\frac{i}{\sqrt{2}} & 0 & -\frac{1}{\sqrt{2}} & 0 & 0 & 0 \\ 0 & \frac{i}{\sqrt{6}} & 0 & \frac{1}{\sqrt{6}} & i\sqrt{\frac{2}{3}} & 0 \end{pmatrix}. \quad (\text{B3})$$

Appendix C: Frequencies of Ba_2MgWO_6

We examined the accuracy of the frequencies obtained by the CCSD method by calculating the frequencies of a $5d^0$ W cluster of nonmagnetic Ba_2MgWO_6 . We used the

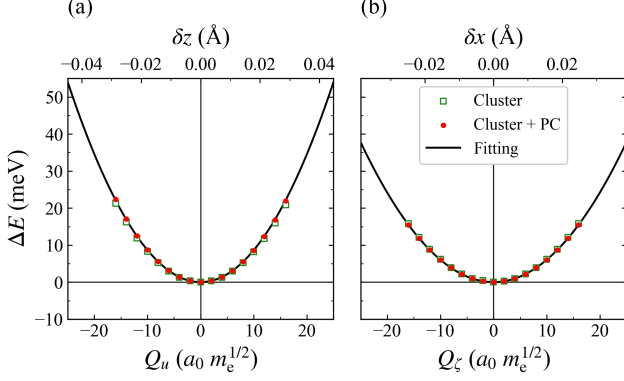


FIG. 10. The total energies of the $5d^0$ W cluster with respect to (a) the E_g and (b) the T_{2g} deformations. The green squares, the red points, and the black solid lines are, respectively, the CCSD data for the W cluster without surrounding point charges, the CCSD data for the W cluster with surrounding point charges (PC), and the fit harmonic potential.

latter because its experimental frequencies are available [83], unlike those of $\text{Ba}_2\text{MgReO}_6$. We constructed the W-based cluster (Fig. 4) from the experimental structure of the crystal [83]. The point charges were W: +2.37, O: -1.25, Ba: +1.82, and Mg: +2.10. The HF and CCSD calculations were performed using the same basis sets and computational approximations as for the Re cluster.

Figure 10 shows the APESs of the $5d^0$ W cluster of Ba_2MgWO_6 . The obtained frequencies are 68.6 meV and 57.3 meV for the E_g and T_{2g} modes, respectively, which are in good agreement with the Raman scattering data of 67.3 meV and 54.4 meV [83].

Appendix D: Vibronic states

Here, we give the dominant contributions for several vibronic wave functions of the DJT model (iii). The ground vibronic state with the largest projection is

$$\begin{aligned}
 |\Psi_{\Gamma_8, -\frac{3}{2}}\rangle &= 0.82 \left| -\frac{3}{2} \right\rangle |0\rangle - 0.45 \left| \Phi_{\Gamma_8, -\frac{3}{2}}^{\Gamma_8 \otimes E} \right\rangle \\
 &\quad - 0.26 \left(\frac{1}{\sqrt{5}} \left| \Phi_{\Gamma_8^{(1)}, -\frac{3}{2}}^{\Gamma_8 \otimes T_2} \right\rangle - \frac{2}{\sqrt{5}} \left| \Phi_{\Gamma_8^{(2)}, -\frac{3}{2}}^{\Gamma_8 \otimes T_2} \right\rangle \right) + \dots,
 \end{aligned}
 \tag{D1}$$

where $|m_j\rangle$ stand for $|j_{\text{eff}} = 3/2, m_j\rangle$ multiplet states, and the symmetrized Γ_8 vibronic basis states with single vibrational excitation are

$$\begin{aligned}
 \left| \Phi_{\Gamma_8, -\frac{3}{2}}^{\Gamma_8 \otimes E} \right\rangle &= \frac{1}{\sqrt{2}} \left(\left| -\frac{3}{2} \right\rangle |1_u\rangle + \left| \frac{1}{2} \right\rangle |1_v\rangle \right), \tag{D2} \\
 \left| \Phi_{\Gamma_8^{(1)}, -\frac{3}{2}}^{\Gamma_8 \otimes T_2} \right\rangle &= i \frac{2}{\sqrt{15}} \left| -\frac{1}{2} \right\rangle |1_\xi\rangle + \frac{i}{\sqrt{5}} \left| \frac{3}{2} \right\rangle |1_\xi\rangle - \frac{2}{\sqrt{15}} \\
 &\quad \times \left| -\frac{1}{2} \right\rangle |1_\eta\rangle + \frac{1}{\sqrt{5}} \left| \frac{3}{2} \right\rangle |1_\eta\rangle + \frac{i}{\sqrt{15}} \left| \frac{1}{2} \right\rangle |1_\zeta\rangle, \tag{D3} \\
 \left| \Phi_{\Gamma_8^{(2)}, -\frac{3}{2}}^{\Gamma_8 \otimes T_2} \right\rangle &= -i \sqrt{\frac{3}{20}} \left| -\frac{1}{2} \right\rangle |1_\xi\rangle + \frac{i}{\sqrt{20}} \left| \frac{3}{2} \right\rangle |1_\xi\rangle + \sqrt{\frac{3}{20}} \\
 &\quad \times \left| -\frac{1}{2} \right\rangle |1_\eta\rangle + \frac{1}{\sqrt{20}} \left| \frac{3}{2} \right\rangle |1_\eta\rangle + i \sqrt{\frac{3}{5}} \left| \frac{1}{2} \right\rangle |1_\zeta\rangle. \tag{D4}
 \end{aligned}$$

$|1_\gamma\rangle$ indicates the vibrational states with one vibrational excitation of mode γ . We constructed these symmetrized vibronic basis sets by using the Clebsch-Gordan coefficients [86].

The lowest Γ_7 vibronic states originate from the E_g vibrationally excited configurations.

$$|\Psi_{\Gamma_7, +\frac{1}{2}}\rangle = 0.79 \left[\frac{1}{\sqrt{2}} \left(\left| \frac{3}{2} \right\rangle |1_u\rangle - \left| -\frac{1}{2} \right\rangle |1_v\rangle \right) \right] + \dots \tag{D5}$$

The first excited Γ_8 vibronic states mainly come from the T_{2g} vibrationally excited states, while containing non-negligible contributions from the E_g vibrationally excited states:

$$\begin{aligned}
 |\Psi'_{\Gamma_8, -\frac{3}{2}}\rangle &= 0.42 \left| \Psi_{\Gamma_8, -\frac{3}{2}}^{\Gamma_8 \otimes E} \right\rangle - 0.05 \left| \Psi_{\Gamma_8^{(1)}, -\frac{3}{2}}^{\Gamma_8 \otimes T_2} \right\rangle \\
 &\quad + 0.63 \left| \Psi_{\Gamma_8^{(2)}, -\frac{3}{2}}^{\Gamma_8 \otimes T_2} \right\rangle + \dots.
 \end{aligned}
 \tag{D6}$$

- [1] W. Witczak-Krempa, G. Chen, Y. B. Kim, and L. Balents, Correlated Quantum Phenomena in the Strong Spin-Orbit Regime, *Annu. Rev. Condens. Matter Phys.* **5**, 57 (2014).
- [2] J. G. Rau, E. K.-H. Lee, and H.-Y. Kee, Spin-Orbit Physics Giving Rise to Novel Phases in Correlated Systems: Iridates and Related Materials, *Annu. Rev. Condens. Matter Phys.* **7**, 195 (2016).
- [3] M. Hermanns, I. Kimchi, and J. Knolle, Physics of the kitaev model: Fractionalization, dynamic correlations, and material connections, *Annu. Rev. Condens. Matter Phys.*

9, 17 (2018).

- [4] H. Takagi, T. Takayama, G. Jackeli, G. Khaliullin, and S. E. Nagler, Concept and realization of Kitaev quantum spin liquids, *Nat. Rev. Phys.* **1**, 264 (2019).
- [5] Y. Motome and J. Nasu, Hunting Majorana Fermions in Kitaev Magnets, *J. Phys. Soc. Jpn.* **89**, 012002 (2020).
- [6] T. Takayama, J. Chaloupka, A. Smerald, G. Khaliullin, and H. Takagi, Spin-Orbit-Entangled Electronic Phases in $4d$ and $5d$ Transition-Metal Compounds, *J. Phys. Soc. Jpn.* **90**, 062001 (2021).
- [7] S. Trebst and C. Hickey, Kitaev materials, *Phys. Rep.*

- 950**, 1 (2022).
- [8] G. V. Chen and C. Wu, Multiflavor Mott insulators in quantum materials and ultracold atoms, *npj Quantum Mater.* **9**, 1 (2024).
- [9] L. V. Pourovskii, D. F. Mosca, L. Celiberti, S. Khmelevskiy, A. Paramekanti, and C. Franchini, Hidden orders in spin-orbit-entangled correlated insulators, *Nat. Rev. Mater.* **10**, 674 (2025).
- [10] P. Santini, S. Carretta, G. Amoretti, R. Caciuffo, N. Magnani, and G. H. Lander, Multipolar interactions in f -electron systems: The paradigm of actinide dioxides, *Rev. Mod. Phys.* **81**, 807 (2009).
- [11] T. Onimaru and H. Kusunose, Exotic Quadrupolar Phenomena in Non-Kramers Doublet Systems — The Cases of $\text{PrT}_2\text{Zn}_{20}$ ($T = \text{Ir, Rh}$) and $\text{PrT}_2\text{Al}_{20}$ ($T = \text{V, Ti}$) —, *J. Phys. Soc. Jpn.* **85**, 082002 (2016).
- [12] M.-T. Suzuki, H. Ikeda, and P. M. Oppeneer, First-principles Theory of Magnetic Multipoles in Condensed Matter Systems, *J. Phys. Soc. Jpn.* **87**, 041008 (2018).
- [13] J. G. Rau and M. J. Gingras, Frustrated Quantum Rare-Earth Pyrochlores, *Annu. Rev. Condens. Matter Phys.* **10**, 357 (2019).
- [14] G. Chen, R. Pereira, and L. Balents, Exotic phases induced by strong spin-orbit coupling in ordered double perovskites, *Phys. Rev. B* **82**, 174440 (2010).
- [15] C. Svoboda, W. Zhang, M. Randeria, and N. Trivedi, Orbital order drives magnetic order in $5d^1$ and $5d^2$ double perovskite Mott insulators, *Phys. Rev. B* **104**, 024437 (2021).
- [16] H. Kubo, T. Ishitobi, and K. Hattori, Electronic origin of ferroic quadrupole moment under antiferroic quadrupole order and finite magnetic moment in $J_{\text{eff}} = \frac{3}{2}$ systems, *Phys. Rev. B* **107**, 235134 (2023).
- [17] C. A. Marjerrison, C. M. Thompson, G. Sala, D. D. Maharaj, E. Kermarrec, Y. Cai, A. M. Hallas, M. N. Wilson, T. J. S. Munsie, G. E. Granroth, R. Flacau, J. E. Greedan, B. D. Gaulin, and G. M. Luke, Cubic Re^{6+} ($5d^1$) Double Perovskites, $\text{Ba}_2\text{MgReO}_6$, $\text{Ba}_2\text{ZnReO}_6$, and $\text{Ba}_2\text{Y}_{2/3}\text{ReO}_6$: Magnetism, Heat Capacity, μSR , and Neutron Scattering Studies and Comparison with Theory, *Inorg. Chem.* **55**, 10701 (2016).
- [18] L. Lu, M. Song, W. Liu, A. P. Reyes, P. Kuhns, H. O. Lee, I. R. Fisher, and V. F. Mitrović, Magnetism and local symmetry breaking in a Mott insulator with strong spin orbit interactions, *Nat. Commun.* **8**, 14407 (2017).
- [19] W. Liu, R. Cong, E. Garcia, A. Reyes, H. Lee, I. Fisher, and V. Mitrović, Phase diagram of $\text{Ba}_2\text{NaOsO}_6$, a Mott insulator with strong spin orbit interactions, *Physica B: Condens. Matter* **536**, 863 (2018).
- [20] K. Willa, R. Willa, U. Welp, I. R. Fisher, A. Rydh, W.-K. Kwok, and Z. Islam, Phase transition preceding magnetic long-range order in the double perovskite $\text{Ba}_2\text{NaOsO}_6$, *Phys. Rev. B* **100**, 041108 (2019).
- [21] D. Hirai and Z. Hiroi, Successive Symmetry Breaking in a $J_{\text{eff}} = 3/2$ Quartet in the Spin-Orbit Coupled Insulator $\text{Ba}_2\text{MgReO}_6$, *J. Phys. Soc. Jpn.* **88**, 064712 (2019).
- [22] D. Hirai, H. Sagayama, S. Gao, H. Ohsumi, G. Chen, T.-h. Arima, and Z. Hiroi, Detection of multipolar orders in the spin-orbit-coupled $5d$ Mott insulator $\text{Ba}_2\text{MgReO}_6$, *Phys. Rev. Res.* **2**, 022063(R) (2020).
- [23] J.-R. Soh, M. E. Merkel, L. Pourovskii, I. Živković, O. Malanyuk, J. Pásztorová, S. Francoual, D. Hirai, A. Urru, D. Tolj, D. Fiore-Mosca, O. Yazyev, N. A. Spaldin, C. Ederer, and H. M. Rønnow, Spectroscopic signatures and origin of hidden order in $\text{Ba}_2\text{MgReO}_6$, *Nat. Commun.* **15**, 10383 (2024).
- [24] T. Muroi, D. Hirai, H. Sagayama, T.-h. Arima, and Z. Hiroi, Magnetic field-induced tetragonal domain alignment and structural distortion in the spin-orbit-coupled insulator $\text{Ba}_2\text{MgReO}_6$, *Phys. Rev. Mater.* **9**, 084415 (2025).
- [25] H. Ishikawa, T. Takayama, R. K. Kremer, J. Nuss, R. Dinnebier, K. Kitagawa, K. Ishii, and H. Takagi, Ordering of hidden multipoles in spin-orbit entangled $5d^1$ Ta chlorides, *Phys. Rev. B* **100**, 045142 (2019).
- [26] A. Mansouri Tehrani, J.-R. Soh, J. Pásztorová, M. E. Merkel, I. Živković, H. M. Rønnow, and N. A. Spaldin, Charge multipole correlations and order in Cs_2TaCl_6 , *Phys. Rev. Res.* **5**, L012010 (2023).
- [27] D. Fiore Mosca, L. V. Pourovskii, B. H. Kim, P. Liu, S. Sanna, F. Boscherini, S. Khmelevskiy, and C. Franchini, Interplay between multipolar spin interactions, Jahn-Teller effect, and electronic correlation in a $J_{\text{eff}} = \frac{3}{2}$ insulator, *Phys. Rev. B* **103**, 104401 (2021).
- [28] A. Mansouri Tehrani and N. A. Spaldin, Untangling the structural, magnetic dipole, and charge multipolar orders in $\text{Ba}_2\text{MgReO}_6$, *Phys. Rev. Mater.* **5**, 104410 (2021).
- [29] R. Englman, *The Jahn-Teller Effect in Molecules and Crystals* (John Wiley & Sons Ltd, London, 1972).
- [30] W. Moffitt and W. Thorson, Vibronic States of Octahedral Complexes, *Phys. Rev.* **108**, 1251 (1957).
- [31] N. Iwahara, V. Vieru, L. Ungur, and L. F. Chibotaru, Zeeman interaction and Jahn-Teller effect in the Γ_8 multiplet, *Phys. Rev. B* **96**, 064416 (2017).
- [32] N. Iwahara, V. Vieru, and L. F. Chibotaru, Spin-orbital-lattice entangled states in cubic d^1 double perovskites, *Phys. Rev. B* **98**, 075138 (2018).
- [33] N. Iwahara, Dynamic Jahn-Teller Phenomena in Heavy Transition Metal Compounds, *J. Phys. Soc. Jpn.* **93**, 121003 (2024).
- [34] H. C. Longuet-Higgins, U. Öpik, M. H. L. Pryce, and R. A. Sack, Studies of the Jahn-Teller Effect. II. The Dynamical Problem, *Proc. R. Soc. A: Math. Phys. Eng. Sci.* **244**, 1 (1958).
- [35] S. Muramatsu and N. Sakamoto, Dynamic Jahn-Teller Vibronic Coupling in Tetragonal Symmetry, *J. Phys. Soc. Jpn.* **44**, 1640 (1978).
- [36] N. Iwahara and L. F. Chibotaru, Vibronic order and emergent magnetism in cubic d^1 double perovskites, *Phys. Rev. B* **107**, L220404 (2023).
- [37] L. J. P. Ament, M. van Veenendaal, T. P. Devereaux, J. P. Hill, and J. van den Brink, Resonant inelastic x-ray scattering studies of elementary excitations, *Rev. Mod. Phys.* **83**, 705 (2011).
- [38] K. Gilmore, Quantifying vibronic coupling with resonant inelastic X-ray scattering, *Phys. Chem. Chem. Phys.* **25**, 217 (2023).
- [39] M. Mitrano, S. Johnston, Y.-J. Kim, and M. P. M. Dean, Exploring quantum materials with resonant inelastic x-ray scattering, *Phys. Rev. X* **14**, 040501 (2024).
- [40] F. M. F. de Groot, M. W. Haverkort, H. Elnaggar, A. Juhin, K.-J. Zhou, and P. Glatzel, Resonant inelastic x-ray scattering, *Nat. Rev. Methods Primers* **4**, 45 (2024).
- [41] A. E. Taylor, S. Calder, R. Morrow, H. L. Feng, M. H. Upton, M. D. Lumsden, K. Yamaura, P. M. Woodward, and A. D. Christianson, Spin-Orbit Coupling Controlled $J = 3/2$ Electronic Ground State in $5d^3$ Oxides, *Phys.*

- Rev. Lett.* **118**, 207202 (2017).
- [42] J. Kim, J. Chaloupka, Y. Singh, J. W. Kim, B. J. Kim, D. Casa, A. Said, X. Huang, and T. Gog, Dynamic Spin Correlations in the Honeycomb Lattice Na_2IrO_3 Measured by Resonant Inelastic x-Ray Scattering, *Phys. Rev. X* **10**, 021034 (2020).
- [43] P. Warzanowski, M. Magnaterra, P. Stein, G. Schlicht, Q. Faure, C. J. Sahle, T. Lorenz, P. Becker, L. Bohatý, M. Moretti Sala, G. Monaco, P. H. M. van Loosdrecht, and M. Grüninger, Electronic excitations in $5d^4 J = 0$ Os^{4+} halides studied by resonant inelastic x-ray scattering and optical spectroscopy, *Phys. Rev. B* **108**, 125120 (2023).
- [44] M. Magnaterra, J. Attig, L. Peterlini, M. Hermanns, M. H. Upton, J. Kim, L. Prodan, V. Tsurkan, I. Kézsmárki, P. H. M. van Loosdrecht, and M. Grüninger, Quasimolecular $J_{\text{tet}} = 3/2$ Moments in the Cluster Mott Insulator GaTa_4Se_8 , *Phys. Rev. Lett.* **133**, 046501 (2024).
- [45] J. Okamoto, G. Shibata, Y. S. Ponosov, H. Hayashi, K. Yamaura, H. Y. Huang, A. Singh, C. T. Chen, A. Tanaka, S. V. Streltsov, D. J. Huang, and A. Fujimori, Spin-orbit-entangled state of $\text{Ba}_2\text{CaOsO}_6$ studied by O K-edge resonant inelastic X-ray scattering and Raman spectroscopy, *npj Quant. Mater.* **10**, 44 (2025).
- [46] F. I. Frontini, C. J. S. Heath, B. Yuan, C. M. Thompson, J. Greedan, A. J. Hauser, F. Y. Yang, M. P. M. Dean, M. H. Upton, D. M. Casa, and Y.-J. Kim, Resonant inelastic x-ray scattering investigation of Hund's and spin-orbit coupling in $5d^2$ double perovskites, *Phys. Rev. B* **112**, 165103 (2025).
- [47] F. I. Frontini, G. H. J. Johnstone, N. Iwahara, P. Bhattacharyya, N. A. Bogdanov, L. Hozoi, M. H. Upton, D. M. Casa, D. Hirai, and Y.-J. Kim, Spin-Orbit-Lattice Entangled State in A_2MgReO_6 ($\text{A} = \text{Ca}, \text{Sr}, \text{Ba}$) Revealed by Resonant Inelastic X-Ray Scattering, *Phys. Rev. Lett.* **133**, 036501 (2024).
- [48] S. Agrestini, F. Borgatti, P. Florio, J. Frassinetti, D. Fiore Mosca, Q. Faure, B. Detlefs, C. J. Sahle, S. Francoal, J. Choi, M. Garcia-Fernandez, K.-J. Zhou, V. F. Mitrović, P. M. Woodward, G. Ghiringhelli, C. Franchini, F. Boscherini, S. Sanna, and M. Moretti Sala, Origin of Magnetism in a Supposedly Nonmagnetic Osmium Oxide, *Phys. Rev. Lett.* **133**, 066501 (2024).
- [49] I. Živković, J.-R. Soh, O. Malanyuk, R. Yadav, F. Pisani, A. M. Tehrani, D. Tolj, J. Pasztorova, D. Hirai, Y. Wei, W. Zhang, C. Galdino, T. Yu, K. Ishii, A. Demuer, O. V. Yazyev, T. Schmitt, and H. M. Rønnow, Dynamic Jahn-Teller effect in the strong spin-orbit coupling regime, *Nat. Commun.* **15**, 8587 (2024).
- [50] N. Iwahara, J.-R. Soh, D. Hirai, I. Živković, Y. Wei, W. Zhang, C. Galdino, T. Yu, K. Ishii, F. Pisani, O. Malanyuk, T. Schmitt, and H. M. Rønnow, Persistent quantum vibronic dynamics in a $5d^1$ double perovskite oxide, *Phys. Rev. B* **112**, 104104 (2025).
- [51] L. Xu, N. A. Bogdanov, A. Princep, P. Fulde, J. van den Brink, and L. Hozoi, Covalency and vibronic couplings make a nonmagnetic $j = 3/2$ ion magnetic, *npj Quantum Mater.* **1**, 16029 (2016).
- [52] D. Fiore Mosca, C. Franchini, and L. V. Pourovskii, Interplay of superexchange and vibronic effects in the hidden order of $\text{Ba}_2\text{MgReO}_6$ from first principles, *Phys. Rev. B* **110**, L201101 (2024).
- [53] A. I. Krylov, Equation-of-Motion Coupled-Cluster Methods for Open-Shell and Electronically Excited Species: The Hitchhiker's Guide to Fock Space, *Annu. Rev. Phys. Chem.* **59**, 433 (2008).
- [54] K. Snegov and O. Christiansen, Excited state coupled cluster methods, *WIREs Comput. Mol. Sci.* **2**, 566 (2012).
- [55] R. J. Bartlett, Coupled-cluster theory and its equation-of-motion extensions, *WIREs Comput. Mol. Sci.* **2**, 126 (2012).
- [56] N. Orms and A. I. Krylov, Singlet-triplet energy gaps and the degree of diradical character in binuclear copper molecular magnets characterized by spin-flip density functional theory, *Phys. Chem. Chem. Phys.* **20**, 13127 (2018).
- [57] P. Pokhilko, E. Epifanovsky, and A. I. Krylov, General framework for calculating spin-orbit couplings using spinless one-particle density matrices: Theory and application to the equation-of-motion coupled-cluster wave functions, *J. Chem. Phys.* **151**, 034106 (2019).
- [58] M. Alessio and A. I. Krylov, Equation-of-Motion Coupled-Cluster Protocol for Calculating Magnetic Properties: Theory and Applications to Single-Molecule Magnets, *J. Chem. Theory Comput.* **17**, 4225 (2021).
- [59] M. Alessio, S. Kotaru, G. Giudetti, and A. I. Krylov, Origin of Magnetic Anisotropy in Nickelocene Molecular Magnet and Resilience of Its Magnetic Behavior, *J. Phys. Chem. C* **127**, 3647 (2023).
- [60] S. Kähler, A. Cebreiro-Gallardo, P. Pokhilko, D. Casanova, and A. I. Krylov, State-Interaction Approach for Evaluating g-Tensors within EOM-CC and RAS-CI Frameworks: Theory and Benchmarks, *J. Phys. Chem. A* **127**, 8459 (2023).
- [61] S. Eversdijk, Coupled cluster treatment of magnetic exchange interactions in cuprates, master's thesis, KU Leuven (2025).
- [62] S. Sugano, Y. Tanabe, and H. Kamimura, *Multiplets of Transition-Metal Ions in Crystals* (Academic Press, New York, 1970).
- [63] E. B. Wilson, Jr., J. C. Decius, and P. C. Cross, *Molecular Vibrations, The theory of infrared and Raman vibrational spectra* (Dover Publication Inc., New York, 1980).
- [64] U. Öpik and M. H. L. Pryce, Studies of the Jahn-Teller Effect. I. A Survey of the Static Problem, *Proc. R. Soc. A: Math. Phys. Eng. Sci.* **238**, 425 (1957).
- [65] A. D. Liehr, Topological aspects of the conformational stability problem. part i. degenerate electronic states I, *J. Phys. Chem.* **67**, 389 (1963).
- [66] S. V. Streltsov and D. I. Khomskii, Jahn-Teller Effect and Spin-Orbit Coupling: Friends or Foes?, *Phys. Rev. X* **10**, 031043 (2020).
- [67] S. V. Streltsov, F. V. Temnikov, K. I. Kugel, and D. I. Khomskii, Interplay of the Jahn-Teller effect and spin-orbit coupling: The case of trigonal vibrations, *Phys. Rev. B* **105**, 205142 (2022).
- [68] E. Epifanovsky *et al.*, Software for the frontiers of quantum chemistry: An overview of developments in the Q-Chem 5 package, *J. Chem. Phys.* **155**, 084801 (2021).
- [69] K. G. Bramnik, H. Ehrenberg, J. K. Dehn, and H. Fuess, Preparation, crystal structure, and magnetic properties of double perovskites M_2MgReO_6 ($\text{M} = \text{Ca}, \text{Sr}, \text{Ba}$), *Solid State Sci.* **5**, 235 (2003).
- [70] P. Pollak and F. Weigend, Segmented Contracted Error-Consistent Basis Sets of Double- and Triple- ζ Valence

- Quality for One- and Two-Component Relativistic All-Electron Calculations, *J. Chem. Theory Comput.* **13**, 3696 (2017).
- [71] T. H. J. Dunning, Gaussian basis sets for use in correlated molecular calculations. i. the atoms boron through neon and hydrogen, *J. Chem. Phys.* **90**, 1007 (1989).
- [72] W. J. Stevens, H. Basch, and M. Krauss, Compact effective potentials and efficient shared-exponent basis sets for the first- and second-row atoms, *J. Chem. Phys.* **81**, 6026 (1984).
- [73] W. J. Stevens, M. Krauss, H. Basch, and P. G. Jasien, Relativistic compact effective potentials and efficient, shared-exponent basis sets for the third-, fourth-, and fifth-row atoms, *Can. J. Chem.* **70**, 612 (1992).
- [74] B. P. Pritchard, D. Altarawy, B. Didier, T. D. Gibson, and T. L. Windus, A New Basis Set Exchange: An Open, Up-to-Date Resource for the Molecular Sciences Community, *J. Chem. Inf. Model.* **59**, 4814 (2019).
- [75] H. Bolvin and J. Autschbach, Relativistic methods for calculating electron paramagnetic resonance (epr) parameters, in *Handbook of Relativistic Quantum Chemistry*, edited by W. Liu (Springer Berlin Heidelberg, Berlin, Heidelberg, 2017) pp. 725–763.
- [76] M. Iliáš and T. Saue, An infinite-order two-component relativistic Hamiltonian by a simple one-step transformation, *J. Chem. Phys.* **126**, 064102 (2007).
- [77] W. Liu and D. Peng, Exact two-component hamiltonians revisited, *J. Chem. Phys.* **131**, 031104 (2009).
- [78] M. Nooijen and R. J. Bartlett, Equation of motion coupled cluster method for electron attachment, *J. Chem. Phys.* **102**, 3629 (1995).
- [79] P. Pokhilko and A. I. Krylov, Quantitative el-sayed rules for many-body wave functions from spinless transition density matrices, *J. Phys. Chem. Lett.* **10**, 4857 (2019).
- [80] A. Carreras, H. Jiang, P. Pokhilko, A. I. Krylov, P. M. Zimmerman, and D. Casanova, Calculation of spin-orbit couplings using rasci spinless one-particle density matrices: Theory and applications, *J. Chem. Phys.* **153**, 214107 (2020).
- [81] J. J. Sakurai, *Advanced Quantum Mechanics* (Addison-Wesley, Massachusetts, 1967).
- [82] J. P. Clancy, N. Chen, C. Y. Kim, W. F. Chen, K. W. Plumb, B. C. Jeon, T. W. Noh, and Y.-J. Kim, Spin-orbit coupling in iridium-based $5d$ compounds probed by x-ray absorption spectroscopy, *Phys. Rev. B* **86**, 195131 (2012).
- [83] J. Pásztorová, W. H. Bi, R. Gaal, K. Krämer, I. Živković, and H. M. Rønnow, Structure, heat capacity and Raman spectra of Ba_2MgWO_6 single crystals grown in BaCl_2 - MgCl_2 flux, *J. Solid State Chem.* **326**, 124184 (2023).
- [84] M. C. M. O'Brien, The dynamic Jahn-Teller effect in octahedrally co-ordinated d^9 ions, *Proc. R. Soc. A: Math. Phys. Eng. Sci.* **281**, 323 (1964).
- [85] Repository at <https://opac.ll.chiba-u.jp/da/curator/900123734/?lang=1>.
- [86] G. F. Koster, J. O. Dimmock, R. G. Wheeler, and H. Statz, *Properties of the thirty-two point groups* (MIT press, Massachusetts, 1963).